Met. Mater. Int., Vol. 23, No. 5 (2017), pp. 974~983
doi: 10.1007/s12540-017-6656-2

Influence of Fe Addition on Microstructure and Properties of Cu-Ag Composite

Xiaowei Zuo[1,2,*], Jianzheng Zhu[1,3], Bailing An[1,3], Ke Han[4], Rui Li[1,3], and Engang Wang[1,2,*]

[1]Key Laboratory of Electromagnetic Processing of Materials (Ministry of Education), Northeastern University, Shenyang 110819, China
[2]School of Metallurgy, Northeastern University, Shenyang 110819, China
[3]School of Materials Science and Engineering, Northeastern University, Shenyang 110819, China
[4]National High Magnetic Field Laboratory, Florida State University, Tallahassee 32310, FL, USA

(received date: 21 September 2016 / accepted date: 10 January 2017)

We investigated the effects of Fe content on microstructure and properties in as-cast and as-drawn Cu-(5.1-x) vol%Ag-x vol%Fe alloys. In microscale, increasing Fe content first refined and then coarsened Cu dendrites. In nanoscale, the size and length of Ag precipitates in Fe-doped alloys were smaller than the size and length of Ag precipitates in Fe-free alloy, and the γ-Fe precipitates in Cu-2.9 vol%Ag-2.4 vol%Fe alloy were finer than the γ-Fe precipitates in Cu-5.1 vol%Fe alloy. The maximum hardness in as-cast Cu-Ag-Fe alloys was found in the Cu-2.9 vol%Ag-2.4 vol%Fe alloy. With increasing drawing strain, both ultimate tensile strength and hardness of Cu-Ag-Fe composites were increased. Simulation data among the relative volume fractions of Fe, hardness and electrical conductivity showed that, as the relative value approached 40%, the Cu-Ag-Fe composite displayed greater hardness than other samples. As a small amount of Ag was replaced by Fe, the electrical conductivity decreased significantly with a descending slope of approximately 3%IACS (International Annealed Copper Standard) per vol% Fe. As 47 vol%Ag was replaced by Fe, however, the electrical conductivity decreased by 51% and remained almost invariable with further increasing Fe content. After annealing at 450 °C for 4 h, the electrical conductivity of the Cu-2.9 vol%Ag-2.4 vol%Fe composite was elevated up to 68.3%IACS from 38.5%IACS.

Key words: Cu-Ag-Fe alloy, drawing, strength, electrical conductivity, nanostructured materials

1. INTRODUCTION

Cu-based in situ composites have found applications in high-field magnets [1,2] and robotics [3] because of their excellent combination of strength and electrical conductivity. In those composites, a body-centered cubic (bcc) transition metal (Nb, Fe, Cr and V) and/or face-centered cubic (fcc) Ag are mixed and deformed with a Cu matrix [4-11]. A Cu-Nb composite with an ultimate tensile strength (UTS) of 2.2 GPa and a Cu-Ag composite with a UTS of 1.5 GPa have been reported [11,12]. Although Cu-Nb composites resist elevated temperatures and display thermal stability compared to Cu-Ag composites during their service life [13,14], they are more difficult to fabricate than Cu-Ag composites because of the high melting point. Cu-Ag composites have been applied as winding conductors because of the good compatibility and low melting temperature. A series of Cu-Ag alloys with different Ag contents was studied in terms of strength and electrical conductivity [15,16]. This sort of Cu-Ag alloy is composed of proeutectic Cu with nanostructured Ag precipitates and eutectic colonies that surrounded proeutectic Cu-like networks [17,18]. The strength of the Cu-Ag composite originated from the high interface density after massive deformation and presented as Hall-Petch strengthening, which was similar to that of Cu-bcc composites [7,12,19]. The relationship between microstructure and properties revealed that the nanosized Ag precipitate in proeutectic Cu played important roles [17,18,20]. It is desirable to refine the spacing between Ag precipitates and reduce the Ag composition dissolved in proeutectic Cu for the optimization of the combined properties of Cu-Ag alloys. Optimization of the precipitation behavior of Ag was focused on by adjusting the solidification microstructure [18,21], seeking optimum thermomechanical processing [1,14,21,22] and subjecting the Ag to severe plastic deformation processing [14,21-24], etc. The UTS of 1000 MPa and electrical conductivity of 80%IACS (International Annealed Copper Standard) were achieved in the Cu-24 wt% Ag wires [15], and the UTS of 1050 MPa and electrical conductivity of 75%IACS have been reported in Cu-24 wt% Ag sheets [11].

The cost performance and workability of the alloy were involved as well. Cu-6 wt% Ag alloy that was superior to the Cu-24 wt% Ag alloy has been achieved successfully, which was proposed to resolve the issues [25]. Discontinuous and

*Corresponding authors: zuoxw@epm.neu.edu.cn, egwang@mail.neu.edu.cn

continuous precipitation were reported during the aging treatment, and they were dependent on Ag composition [26,27], aging temperatures [28], and the addition of third elements [29-31]. By tuning the solidification microstructure and the aging temperature, the size and spacing of Ag precipitates were optimized, leading to simultaneous increases in both microhardness and electrical conductivity in the Cu-6wt%Ag composite [32]. In the Cu-Ag system, Cu and Ag have similar slip systems, which limits the further increase in strength [33,34]. Therefore, enhancement of properties of Cu-6 wt% Ag alloy is still an open question.

Compared to Nb, Fe has a lower melting temperature and a similar bcc crystal structure. The Cu-Fe alloy was also applied as the outermost coils of the Bitter disks for the 35.5 T hybrid magnet [35] and presented superior thermal stability with elevated temperatures [36,37]. Numerous studies were performed on the Cu-Fe system in terms of strengthening and coarsening [8,37-39], precipitation of Fe [40-42], martensitic phase transformation [43-45], and magnetic properties [46], where Fe precipitation from the Cu matrix was paid more attention because of the large impurity-scattering impact from the dissolved Fe in Cu [38,42,47,48]. Cu and Fe have different slip systems during co-deformation, which produces dislocations along the Cu/Fe interface and increases the strength [41,49]. Moreover, Fe precipitation also blocks movements of dislocations and strengthens the Cu matrix [41,42]. Therefore, the researchers expected to decrease dissolved Fe in the Cu and increase the Fe precipitation, which can simultaneously increase the strength and electrical conductivity of the Cu-Fe alloy.

To increase the strength of the Cu-Ag alloy by introducing obstacles to block the motion of dislocations, some researchers investigated the Cu-Ag-Fe ternary system, where fcc-fcc (and/or bcc) co-deformation and the interaction between Ag and Fe were involved [50-53]. In most of the previous research, Ag was selected to improve the precipitation of Fe from the Cu matrix in a low-cost Cu-Fe alloy [50,54-56]. The addition of Ag was capable of refining Fe dendrites and promoting precipitation of Fe from the Cu matrix [57]. However, Cu-6wt%Ag-(2-6) wt%Fe alloys were studied [51,52], and the results indicated that the strengthening from Fe was believed to occur as a result of a dislocation mechanism or an interface obstacle mechanism [52]. The Cu–Ag system exhibited excellent co-de-formation capability. However, the co-deformation of the Ag-Fe system was scale-dependent [51]. Although Fe strengthened the Cu matrix and had some positive influence on Ag precipitation from the Cu matrix, more evidence should be provided to analyze the interaction among Cu, Ag and Fe and provide a deeper insight into the microstructure–properties relationship after Ag has been replaced by Fe.

The purpose of our current investigation is threefold. First, we are interested in investigating the influence of equivalent-volume Ag that has been replaced by Fe on the structure and properties of the Cu-Ag composite. Macrostructure, microstructure, and nanostructure in this series of alloys have been systematically studied. The electrical conductivity, hardness and UTS of the Cu-Ag-Fe alloy are discussed in response to the microstructural evolution with different Fe substitutions, which was helpful to demonstrate the contributions of both Ag and Fe to the electrical conductivity and hardness. Second, high-temperature quenching was used during solidification to keep high-temperature phases as much as possible, which leads to the conclusions on the effect of Fe addition rather than the precipitation of both Ag and Fe. Lastly, the impact of heat treatment on the microhardness and electrical conductivity of the Cu-Ag-Fe composite was also presented to improve the combined properties because the increasing electrical resistivity owing to the dissolved Fe in the Cu matrix might be one of the important issues, and heat treatment was beneficial to promote the precipitation of Fe, decreasing the electrical resistivity [40-42].

In this work, we replaced an equivoluminal Ag in Cu-5.1 vol%Ag reference alloy with Fe instead of the addition of Fe into the Cu-6wt%Ag reference alloy [51,52]. The alloys with different Fe substitutions were solidified and cold-rolled into composites. The influence of the Fe content on the microstructure evolution of the Cu-Ag-Fe alloy was investigated by optical microscopy (OM) and a scanning electron microscope (SEM) equipped with an energy dispersive X-ray spectrometer (EDS) detector, X-ray diffraction (XRD) and a transmission electron microscope (TEM).

2. EXPERIMENTAL PROCEDURE

In the designated five alloys, Fe was substituted for Ag while the Cu content remained at 94.9 vol% (Table 1). Because the melting temperature of Fe is higher than the melting tem-

Table 1. Nominal chemistry of designated Cu-Ag-Fe alloys and volume fraction of individual component, where *V* indicates the volume fraction

Nominal Composition	V_{Cu} (%)	V_{Ag} (%)	V_{Fe} (%)	$V_{Fe}/(V_{Ag}+V_{Fe})$ (%)
Cu-6 wt% Ag	94.9	5.1	-	0
Cu-5.3 wt%Ag-0.5 wt%Fe	94.9	4.5	0.6	12%
Cu-4.7 wt%Ag-1 wt%Fe	94.8	3.9	1.3	25%
Cu-3.4 wt%Ag-2 wt%Fe	94.7	2.9	2.4	47%
Cu-2.5 wt%Ag-3 wt%Fe	94.9	1.5	3.6	71%
Cu-4.5 wt%Fe	94.9	-	5.1	100%

Note: relative volume fraction of Fe = $V_{Fe}/(V_{Ag}+V_{Fe})$

perature of both Cu and Ag, a Cu-10wt%Fe master alloy received from ACI Alloys, Inc., USA, was used to lower the temperature of the liquid melt. Each Cu-Ag-Fe alloy was induction-melted under an Ar atmosphere from oxygen-free Cu, electrolytic Ag, and Cu-10wt%Fe alloy. During casting, thermocouples were used to monitor the temperatures of both the liquid melt and the alloy in the crucible before quenching. The melt was poured into a graphite crucible and then quenched into water once the melt reached 900 °C. The as-cast alloy with 25 mm diameter was machined to 22 mm in diameter and swaged to 12 mm in diameter. The swaged alloy was then cold-drawn to different diameters at room temperature. The drawing strain value (η) was estimated by $\eta=2\times\ln(d_0/d)$, where d_0 and d are the initial and final diameters, respectively. The maximum drawing rate, η, reached 5.1. In addition, previous results indicate that an aging temperature of 400-475 °C was optimized for improving the properties of the Cu-Ag alloys because of the precipitation reaction of Ag [28,34,58]. We used isothermal heat treatment at the temperature of 450 °C for 0.5-2 h in Cu-Ag-Fe composites at the drawing rate of 5.1 to improve the electrical conductivity of the Cu-Ag-Fe composites.

The as-cast and as-drawn samples were sectioned and polished using standard metallographic methods. After they were etched in a solution of 2 g $FeCl_3$, 5 ml HCl and 100 ml C_2H_5OH, the macrostructure of the as-cast samples was observed using a DW/T-400 stereoscope. The microstructure of as-cast and as-drawn samples was observed using OM and SEM equipped with an EDS detector. XRD was performed using Cu K_α radiation. Foils for TEM were prepared by twin jet-polishing and observed on an FEI Tecnai $G^2$20 conventional TEM with an EDS detector operated at 200 kV. Vickers hardness determinations were carried out using a diamond indenter under a load of 2 kg for a dwelling time of 10 s. Tensile tests were performed at a rate of 10^{-3} s^{-1} at room temperature. Electrical resistivity measurements were carried out at room temperature using a four-point-probe method. The resistivity data were divided by electrical resistivity of pure Cu (1.7241×10^{-8}W×m =100%IACS, thus converting into electrical conductivity.

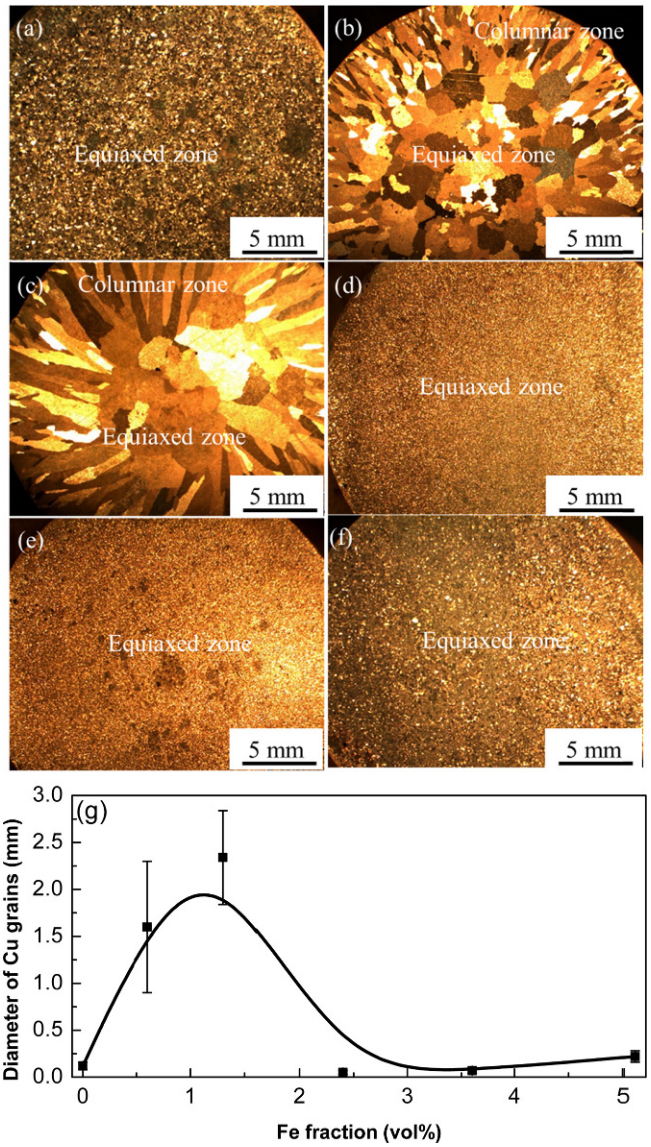

Fig. 1. Macrostructure of: (a) Cu-5.1 vol%Ag, (b) Cu-4.5 vol%Ag-0.6 vol%Fe, (c) Cu-3.9 vol%Ag-1.3 vol%Fe, (d) Cu-2.9 vol%Ag-2.4 vol%Fe, (e) Cu-1.5 vol%Ag-3.6 vol%Fe, and (f) Cu-5.1 vol%Fe alloys. (g) Cu grain size of Cu-Ag-Fe alloys plotted with respect to Fe content.

3. RESULTS

3.1. Microstructure evolution of as-cast Cu-Ag-Fe alloys

The macrostructure examination reveals shape and distribution of grains, which is used to control the quality of initial materials. Fine equiaxed grains are observed in the Cu-5.1 vol%Ag alloy (Fig. 1(a)), which is different from the macrostructure of the conventional as-cast alloy. The conventional macrostructure of the as-cast ingots is composed of coarse column grains outside and equiaxed grains inside [32]. The difference in the macrostructure might be related to the effect of high-temperature quenching on both the nucleation and the growth of grains. The quenching might have resulted in high nucleation rates and low growth rates [59], so that refined Cu grains are formed (Fig. 1(a)). In alloys with less than 2.4 vol%Fe, a conventional macrostructure containing the coarsened columnar and equiaxed grains was observed (Figs. 1(b) and 1(c)). Fe additions increased the melting point so that the alloys started to solidify before quenching, leading to a conventional cast macrostructure to be accelerated. As Fe content was greater than 2.4 vol% (Fig. 1(d)), where the volume fraction of Fe was almost equivalent to or slightly lower than the volume fraction of the Ag (Table 1, the relative volume fraction of Fe is 47%), the nucleation and growth of Cu crystals were changed because the primary Fe was formed earlier than the Cu crystals during solidification. The formed primary Fe particles (which are shown in Fig. 3) might act as nucleation sites for Cu grains and refine

the Cu grains. With the further increase in Fe content (Figs. 1(e) and (f)), equiaxial Cu grains were reserved even when the Fe content was up to 5.1 vol% and Ag was free. The size of the Cu grains shows a similar dependence of the Fe fraction, as shown in Fig. 1(g). We concluded that the evolution of Cu grains was dependent on the relative volume fraction of Fe (estimated by $V_{Fe}/(V_{Ag}+V_{Fe})$). When the Fe content less than approximately 2.4 vol% was substituted by Fe, Fe might accelerate the growth of columnar grains in the Cu-Ag alloy, coarsening the Cu grains.

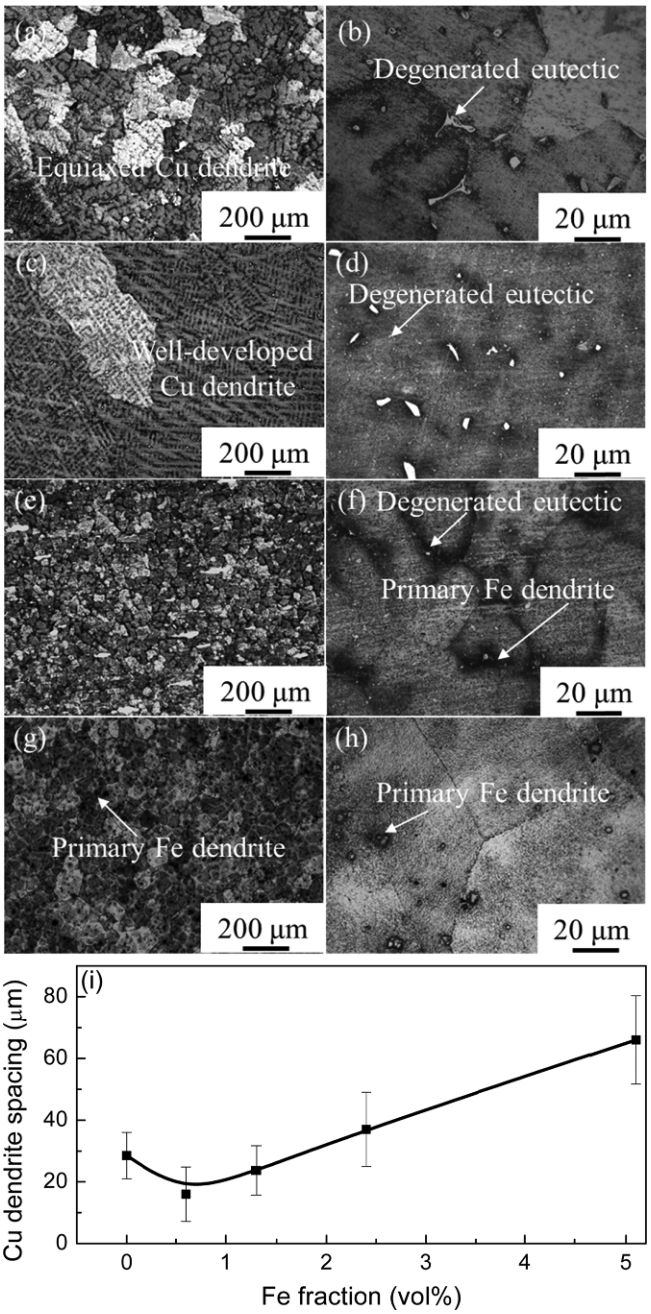

Fig. 2. OM microstructure of: (a, b) Cu-5.1 vol%Ag, (c, d) Cu-4.5 vol%Ag-0.6 vol%Fe, (e, f) Cu-2.9 vol%Ag-2.4 vol%Fe, (g, h) Cu-5.1 vol%Fe alloys, and (i) the spacing between Cu dendrites in Cu-Ag-Fe alloys plotted as the Fe content.

When the Fe content was greater than 2.4 vol%, however, Fe increased the heterogeneous nucleation of Cu crystals, refining the Cu grains.

In microscale, each Cu grain represents a single-crystal that has a different orientation from the orientation of adjacent grains. For Cu grains in Cu-5.1 vol%Ag alloy, degenerated eutectics (Fig. 2(b)) are distributed among equiaxed Cu dendrites (Fig. 2(a)), like the degenerated eutectics observed in previous work [34]. With increasing Fe content, well-developed Cu dendrites (Fig. 2(c)) and a fine degenerated eutectic are found (Fig. 2(d)). With further increasing Fe, equiaxed Cu dendrites (Fig. 2(e)), fine degenerated eutectic and primary Fe dendrites (Fig. 2(f)) are observed in Cu-2.9 vol%Ag-2.4 vol%Fe alloy because of the higher solid phase temperature of Fe. In the Cu-5.1 vol%Fe alloy, both primary spherical Fe dendrites and equiaxed Cu dendrites are found in Figs. 2(g) and 2(h). The spacing of Cu dendrites in Fig. 2(i) decreases first, then reaches its minimum value at the containing-0.6 vol%Fe alloy, and increases further with increasing Fe content.

With decreasing temperature, the solubility of Ag and Fe in the Cu matrix decreases, leading to the formation of secondary Ag and Fe precipitates from the Cu matrix. The secondary Ag and Fe precipitates are formed as a result of a solid-state phase transformation instead of a liquid-solid transformation. Rod-like Ag precipitates are found in the Cu-5.1 vol%Ag alloy (Fig. 3(a)). In both Cu-2.9 vol%Ag-2.4 vol%Fe alloy and Cu-5.1 vol%Fe alloy, the two kinds of Fe particles are found to be spherical (Figs. 3(b) and 3(c)) and twin-like Fe (Figs. 3(b) and 3(d)). Spherical Fe particles were thought to be primary α-Fe particles, and the twin-like Fe was thought to be fine γ-Fe precipitate because similar morphology was found in our previous work [42]. The diameter of γ-Fe in Cu-2.9 vol%Ag-2.4 vol%Fe alloy was a little finer than the diameter of γ-Fe in the Cu-5.1 vol%Fe alloy. In the Cu-2.9 vol%Ag-2.4 vol%Fe alloy, rod-like Ag precipitates are also observed (Fig. 3(f)). However, the size and length of Ag precipitates are smaller than the precipitates in the Cu-5.1 vol%Ag alloy. A portion of the Ag precipitates is distributed along the boundary of the primary α-Fe particles (Fig. 3(e)), which shows that Ag is rich in this area close to the primary α-Fe particles. The interaction between Fe and Ag might be responsible for the refining of both Ag precipitates and γ-Fe precipitates.

3.2. The hardness of as-cast Cu-Ag-Fe alloys

Although Cu-5.1 vol%Fe alloy has the same volume fraction of the second phase as the Cu-5.1 vol%Ag alloy, the hardness of the Cu-5.1 vol%Fe alloy is 16% higher than the hardness of the Cu-5.1 vol%Ag alloy (Fig. 4), attributed to Fe having a higher modulus of elasticity than Ag, and Fe refines the microstructure, leading to higher hardening effects from Fe precipitation than from the precipitation of Ag [55,60]. With increasing Fe additions, the hardness of the Cu-Ag-Fe alloys shows a peak at approximately 2.4 vol% Fe. The addition of Fe refined the sizes

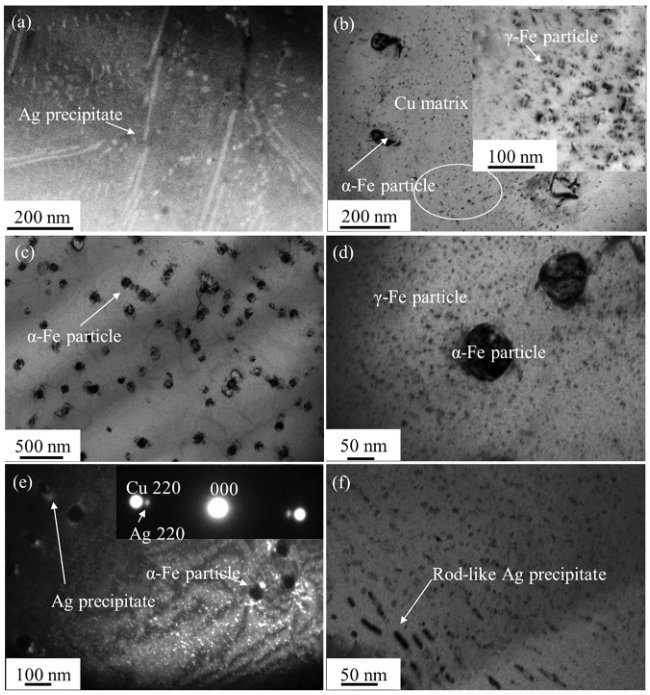

Fig. 3. TEM images showing morphology of: (a) Ag precipitate in Cu-5.1 vol%Ag alloy, (b) α-Fe particles formed during the solidification and γ-Fe (large magnification in inset) formed during the solid state reaction in Cu-5.1 vol%Fe alloy; (c) α-Fe, (d) γ-Fe, (e) dark-field image of Ag precipitate close to α-Fe particles, and (f) rod-like Ag precipitates in Cu-2.9 vol%Ag-2.4 vol%Fe alloy.

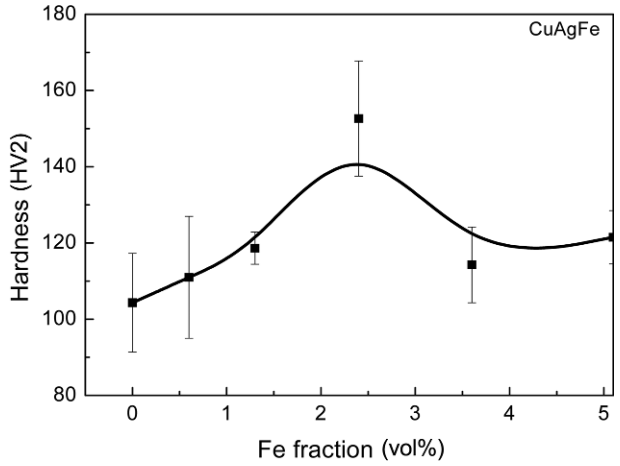

Fig. 4. The hardness of the Cu-Ag-Fe alloy plotted with different Fe fractions.

of both Cu dendrites and degenerated eutectics. Although the spacing of the Cu dendrites reached its minimum value in the containing-0.6 vol%Fe alloy (Fig. 2(i)), nanosized Ag and Fe precipitates might have important roles in hardening the Cu matrix by blocking the motion of dislocation instead of microscale spacing of Cu dendrites [18]. In the containing-2.4 vol%Fe alloy, more Fe precipitates were observed, which might be attributed to the peak of hardness shown in Fig. 4.

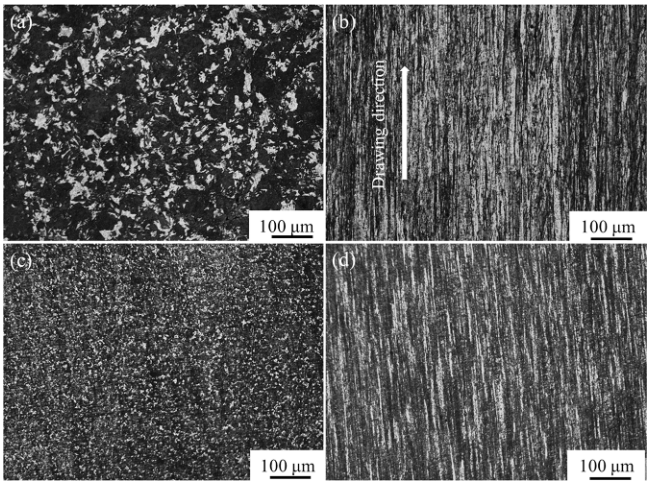

Fig. 5. OM images of Cu-Ag-Fe composites at the drawing rate (η) of 3.5. Images showing microstructure on cross section (a) and longitudinal section (b) of Cu-5.1 vol%Ag composite. Images showing microstructure on cross section (c) and longitudinal section (d) of Cu-2.9 vol%Ag-2.4 vol%Fe composite.

3.3. Microstructure evolution of as-drawn Cu-Ag-Fe composites

In the as-drawn Cu-5.1 vol%Ag composite, Cu grains are deformed and distributed as ribbon-like morphology on a cross section [17,18,25,34,61] (Fig. 5(a)). On the longitudinal section (Fig. 5(a)), the Cu grains are stretched out along the drawing direction. Cu grains in Cu-2.9 vol%Ag-2.4 vol%Fe composite (Figs. 5(c) and 5(d)) have morphology similar to the Cu-Ag composite (Figs. 6(a) and 6(b)), but the Cu-2.9 vol%Ag-2.4 vol%Fe composite has a finer size and a smaller spacing of the deformed Cu grains.

TEM images (Figs. 6(a) and 6(b)) show Cu cell structures as well as Ag and Fe precipitates in the Cu matrix zone. A portion of secondary Ag precipitates is deformed to the fiber-like morphology (Fig. 6(c)), and other portion of Ag precipitates remains as a spherical morphology with a diameter of 30-40 nm (Fig. 6(d)). The similar morphologies of Fe precipitates are found in Figs. 6(e) and 6(f). However, spherical Fe precipitates have a tendency to have a larger aspect ratio, which induces the lath-like morphology (Fig. 6(f)). Abundant dislocations are found close to the precipitates (Fig. 6(a)).

3.4. Properties of as-drawn Cu-Ag-Fe composites

With increasing deformation, hardness (Fig. 7(a)) and ultimate tensile strength (Fig. 7(b)) in all Cu-Ag-Fe composites are enhanced and Cu-2.9 vol%Ag-2.4 vol%Fe composites have larger values. When a small amount of Fe was melted into Cu or Cu-Ag systems, the electrical conductivity was significantly decreased because of the impurity-scattering resistivity to electrons from the dissolved Fe (9.2 μΩcm/wt% Fe [48]), thus increasing the whole resistivity of the composites. We conclude that the addition of Fe increases the mechanical properties but

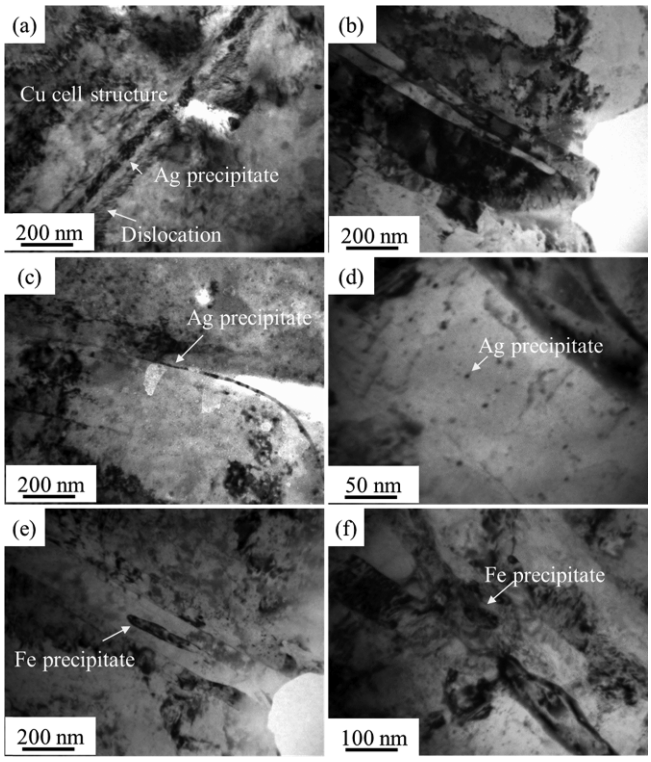

Fig. 6. TEM images of Cu-2.9 vol%Ag-2.4 vol%Fe composite at the drawing rate (η) of 3.8. (a) Morphology of Ag precipitates, (b) morphology of Cu fiber ribbon, (c) and (d) the secondary Ag fiber and the nanoprecipitated Ag particles during the deformation process, (e) and (f) morphology of Fe precipitates during deformation.

decreases the electrical conductivity significantly.

Heat treatment at 450 °C decreases the microhardness (Fig. 8(a)) but increases the electrical conductivity of Cu-Ag-Fe composites (Fig. 8(b)). After annealing at 450 °C for 4 h, the microhardness of the Cu-Ag and Cu-Fe composites decreased significantly but the decreasing tendency of the Cu-Ag-Fe composite was lower (see the relative slope in Fig. 8(a)) owing to the interaction strengthening effect from Ag and Fe. The electrical conductivity of the Cu-2.9 vol%Ag-2.4 vol%Fe composite was up to 68.3%IACS (Fig. 8(b)) from 38.5%IACS. The doubled increase in the electrical conductivity was thought to be caused by the precipitation of Ag and Fe from the Cu matrix [25,34,38,42,51].

4. DISCUSSION

4.1. Microstructure evolution of as-cast Cu-Ag-Fe alloys

The addition of Cr [31,62], Zr [61,62] and rare earth elements [63,64] into the Cu-Ag alloy was capable of refining the Cu dendrites. Huang *et al.* [52] studied the additional 2-6wt%Fe into Cu-6wt%Ag alloy, and the results indicated that Fe particles were not observed in the containing-2wt%Fe alloy, and the increase of the Fe refined the size of the proeutectic Cu dendrites and changed the volume fraction of the Cu dendrites.

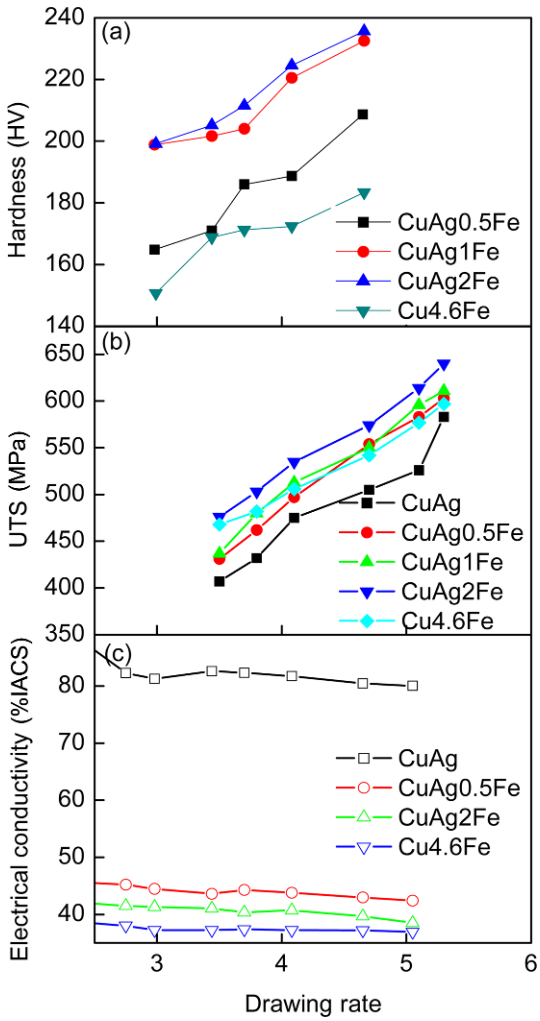

Fig. 7. (a) Hardness, (b) UTS, and (c) electrical conductivity of Cu-Ag-Fe composite as a function of drawing rate.

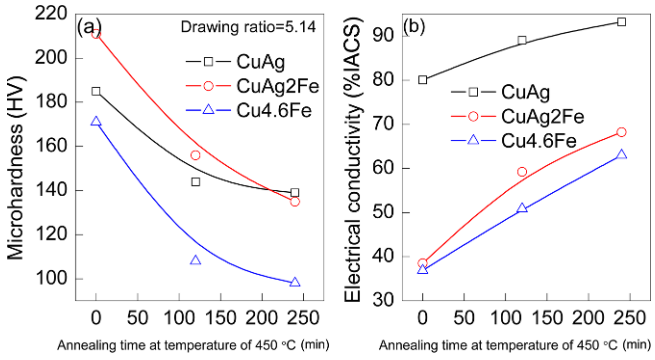

Fig. 8. The relationship between the properties and annealing time in Cu-Ag-Fe composites when η = 5.14; (a) microhardness and (b) electrical conductivity.

However, it was still difficult to conclude that the refining contribution of the proeutectic Cu dendrites was only as a result of the increasing Fe. The refining of grains or dendrites was closely related to the nucleation site and growth. However, den-

drite spacing was dependent on the local solidification time and the diffusion coefficient controlled by the casting temperature, the cooling rate, and the composition, which were possibly responsible for the different tendency resulting from adding Fe into the Cu-Ag alloy [65]. Our results clearly showed that the evolution of Cu dendrites was related to both the solidification path and the comparable volume fraction of minor elements. Sakai *et al.* [25] proposed to superimpose solid solution treatment and 450 °C annealing after a low deformation in the Cu-(1-6) wt%Ag alloy, and the UTS of 1.4 GPa can be achieved. Therefore, solid solution treatment and optimum annealing played important roles in the properties of the Cu-Ag alloy. In this work, high-temperature quenching might introduce some defects, but it clearly presents the microstructural evolution of Fe addition, which is different from previous work [31,61-64]. A small quantity of Fe into the Cu-Ag alloy coarsened Cu grains and promoted the growth of columnar grains (Figs. 1(b) and 1(c)) but refined the size of the Cu dendrites (Fig. 2(c)) because of the increase in heterogeneous nucleation sites [59]. Comparative Fe with Ag changed the nucleation path of the Cu dendrites because a small quantity of Fe was possibly formed as primary dendrites although it was hard to observe them in Fig. 2(e). The refined Cu grains (Fig. 1(d)) and refined equaxied Cu dendrites (Fig. 2(e)) were formed.

4.2. Hardness and strength related to microstructural changes caused by Fe addition

Microstructure in the Cu-Ag-Fe alloys was composed of Cu dendrites dissolved with Ag and Fe, degenerated eutectic, Ag precipitates, and Fe precipitates. Microstructure was neglected in our modeling of hardness because degenerated eutectic and primary Fe dendrites had smaller volume fractions, which have been addressed in previous work [17,18]. Cu dendrites dissolved with Ag and Fe, Ag precipitates and Fe precipitates dominated to harden the Cu matrix [18,66].

The hardness related to the Cu matrix and the Fe precipitation was determined by Eq. (1) [67,68]:

$$HV = HV_0 + k_H d^{-1/2} \quad (1)$$

where HV_0 is the friction stress reported to be near 0 MPa [19,57,69,70], and d is the spacing between Cu dendrites or between precipitates.

Solid solution hardening can be expressed by the following Eq. (2) [71]:

$$HV_{SS} = k\sqrt{\frac{x_a}{3}} \quad (2)$$

where k is a function of the alloying element and lattice parameter change due to added elements [72], and x_a is the Ag or Fe content in the Cu.

The hardness of the Cu-Ag-Fe alloy can be expressed by:

$$HV = k_{HAg} d_{Ag}^{-1/2} V_{Ag} + k_{Cu}\sqrt{\frac{x_{aAg} + x_{aFe}}{3}} + k_{HFe} d_{Fe}^{-1/2} V_{Fe} \quad (3)$$

where the subscripts of Ag and Fe indicate Ag precipitation and Fe precipitation, respectively.

The precipitation hardening in the Cu-5.1 vol%Ag alloy accounted for a large percentage in the overall hardness of the Cu-Ag-Fe alloy because of the nanoprecipitates. Previous studies [53,60,73] indicated that the addition of Ag promoted the precipitation of Fe from the Cu matrix and reduced the solubility of Fe at high temperatures [53,60,73]. Through all of the investigated alloys, the Cu-2.9 vol%Ag-2.4 vol%Fe alloy might have more Fe precipitates with smaller spacing than others (Fig. 3). The Fe precipitates contributed to maximizing the hardness of the Cu-Ag-Fe alloy, as shown in Fig. 4. The third term on the right side of Eq. (3) plays an important role in hardening the Cu matrix. The interaction between Ag and Fe promoted Fe to precipitate from the Cu matrix and hardened the Cu matrix.

Nano Ag precipitation in the Cu matrix is deformed to align along the drawing direction and has a cube-on-cube relationship with the Cu matrix, which shows the compatibility deformation of Ag and Cu because of the same crystallographic structures and slip systems [17,18]. Cu and Fe have different crystallographic structures and different slip systems. Bao *et al.* [51] found that the co-deformation of fcc systems should be scale-dependent. The Fe precipitation deformed during drawing strengthened the Cu matrix (Figs. 6(e) and 6(f)), which might be responsible for the increase in the UTS and hardness of the Cu-Ag-Fe compared to the Cu-Fe composite and the Cu-Ag composite.

4.3. The electrical conductivity of the Cu-Ag-Fe composites

The resistivity of the Cu matrix can be summarized by phonon scattering, impurity scattering, dislocation scattering and interface scattering [74], where impurity scattering plays an important role in the enhancement of the resistivity to the Cu matrix. The resistivity of 9.2 μΩ·cm will be enhanced if 1 wt% Fe is dissolved in the Cu matrix [38]. The resistivity increase per wt% Ag addition is 0.355 μΩm [75]. The dissolved Fe increases the electrical resistivity by one order of magnitude more than the dissolved Ag. In our case, dissolved Fe and Fe precipitates were inclusive, which obviously increased the resistivity, thus reducing the electrical conductivity of the Cu-Ag-Fe composite. The value was higher than the value of the Cu-Fe composite. More Fe precipitates and larger precipitates were found in the Cu-Ag-Fe alloy than in the Cu-5.1 vol%Fe alloy, which indicated that Ag addition promoted the nucleation and growth of Fe precipitation. These results were consistent with previous studies [57,73].

4.4. The evaluation of Fe addition on the properties

To address the effect of Fe addition on the strength and the electrical conductivity of the Cu-Ag composite, microhard-

ness and electrical conductivity were replotted as a function of the volume fraction of Fe addition in (Ag+Fe) phases as the volume fraction of Cu was fixed. The result shown in Fig. 9 demonstrates that the Cu-Ag-Fe composite with approximately a 40% relative volume fraction of Fe has maximum microhardness regardless of which deformation. The increasing ratio of microhardness is up to 21% at the drawing rate of 2.98 (Fig. 9(a)). A small quantity of Fe addition significantly reduces the electrical conductivity of the Cu-Ag-Fe composite regardless of which deformation (Fig. 9(b)), which is a result of dissolved Fe in the Cu matrix [38,47,76,77]. When a 1% relative fraction of Ag was replaced by Fe (the relative fraction of Fe is less than 20%), the electrical conductivity decreased first by approximately 3%IACS. As 47% Ag was replaced by Fe, however, the electrical conductivity decreased by 51% and remained almost invariable. It is necessary to increase both the strength and the electrical conductivity of the Cu-Ag-Fe alloy by promoting the precipitation of Fe from the Cu matrix.

Heat treatment was also applied to optimize the performance of the Cu-Ag-Fe composites. The map between HV and electrical conductivity of Cu-Ag-Fe composites in Fig. 10 indicates

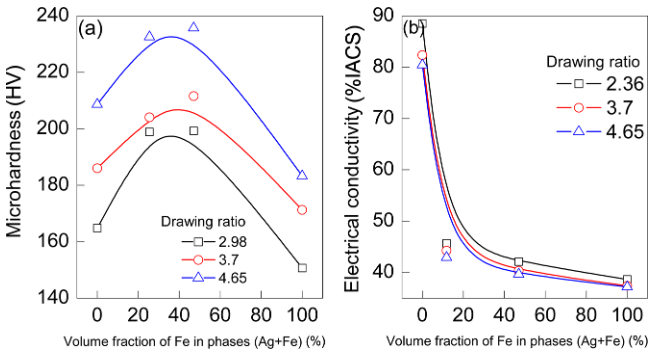

Fig. 9. (a) Microhardness and (b) electrical conductivity as a function of relative volume fraction of Fe.

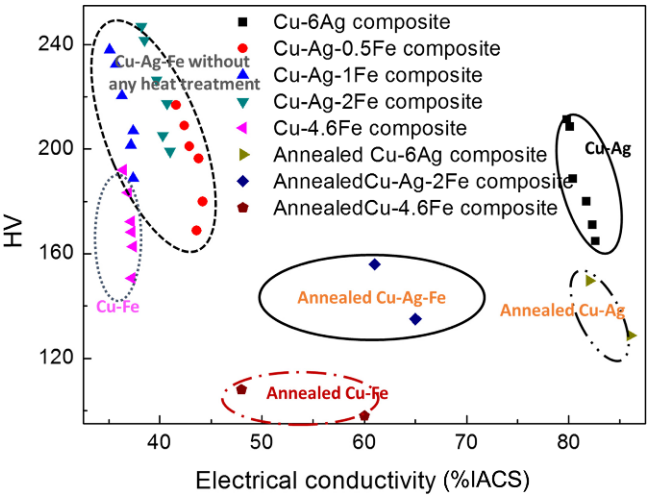

Fig. 10. Hardness versus room temperature electrical conductivity (in % IACS) for Cu-Ag-Fe composites.

that better properties of the Cu-Ag-Fe composite could be achieved by optimizing the thermomechanical process to accelerate the precipitation of both Fe and Ag, indicating that Fe substitution for Ag in the Cu-Ag alloy is meaningful, and it is worthwhile to pay more attention to the Cu-Ag-Fe system.

5. CONCLUSION

(1) With the increase in the substitution of Ag by Fe, the sizes of macro Cu grains in alloys first increased and then decreased. The changes in the Cu grain sizes were dependent on the relative volume fraction of Fe in the total fraction including Ag and Fe. A few Fe additions with less than a 47% relative volume fraction of Fe accelerated the growth of Cu grains in the Cu-Ag alloy, and more than 47% Fe promoted the nucleation of Cu, refining the Cu grains.

(2) With increasing Fe content, the spacing of the Cu dendrites first decreased, reached its minimum value at the Cu-4.5 vol%Ag-0.6 vol%Fe alloy and then increased further. The size and length of the Ag precipitates in the containing-Fe alloys were smaller than the size and length of the Ag precipitates in the Fe-free alloy, and the γ-Fe precipitate in the Cu-2.9 vol%Ag-2.4 vol%Fe alloy was finer than the γ-Fe precipitate in the Cu-5.1 vol%Fe alloy.

(3) With the increasing addition of Fe into the Cu-Ag alloy, the hardness of the Cu-Ag-Fe alloys showed a peak at approximately 2.4 vol% Fe because of the greater hardening contribution from nanoprecipitation of both Fe and Ag.

(4) The addition of Fe increased the mechanical properties but decreased the electrical conductivity significantly. The Cu-Ag-Fe composite with approximately 40% relative volume fraction of Fe showed maximum microhardness. A small quantity of Fe addition reduced the electrical conductivity of the Cu-Ag-Fe composite.

(5) After annealing at 450 °C, the electrical conductivity of the Cu-2.9 vol%Ag-2.4 vol%Fe composite was up to 68.3% IACS from 38.5%IACS because of the precipitation of both Fe and Ag. It is necessary to increase both the strength and the electrical conductivity of the Cu-Ag-Fe alloy by promoting the precipitation of Fe from the Cu matrix.

ACKNOWLEDGMENT

This work was supported by the National Natural Science Foundation of China (Nos. 51474066 and 51004038) and the 111 Project of China (No. B07015).

REFERENCES

1. Y. Sakai, K. Inoue, T. Asano, H. Wada, and H. Maeda, *Appl. Phys. Lett.* **59**, 2965 (1991).
2. K. Han, A. Baca, H. Coe, J. Embury, K. Kihara, H. J. Schneider-Muntau, *et al. IEEE T. Appl. Supercon.* **10**, 1277 (2000).

3. K. Miyake, N. Hanzawa, R. Ninomiya, H. Takahara, S. Kobayashi, and D. Raabe, *Jpn. J. Appl. Phys., Part 2* **39**, 119 (2000).
4. D. Raabe, K. Miyake, and H. Takahara, *Mat. Sci. Eng. A-Struct.* **291**, 186 (2000).
5. D. Raabe and D. Mattissen, *Acta Mater.* **46**, 5973 (1998).
6. D. Raabe and U. Hangen, *Acta Mater.* **44**, 953 (1996).
7. A. Benghalem and D. G. Morris, *Acta Mater.* **45**, 397 (1997).
8. C. Biselli and D. G. Morris, *Acta Mater.* **44**, 493 (1996).
9. S. A. Nikulin, S. O. Rogachev, A. B. Rozhnov, V. I. Pantsyrnyi, N. E. Khlebova, M. Y. Zadorozhnyy, *et al. Compos. Part B-Eng.* **70**, 92 (2015).
10. J. T. Wood, J. D. Embury, and M. F. Ashby, *Acta Mater.* **45**, 1099 (1997).
11. Y. Sakai, K. Inoue, and H. Maeda, *Acta Metall. Mater.* **43**, 1517 (1995).
12. W. A. Spitzig, A. R. Pelton, and F. C. Laabs, *Acta Metall.* **35**, 2427 (1987).
13. L. P. Deng, K. Han, B. S. Wang, X. F. Yang, and Q. Liu, *Acta Mater.* **101**, 181 (2015).
14. S. I. Hong and M. A. Hill, *Mat. Sci. Eng. A-Struct.* **264**, 151 (1999).
15. Y. Sakai, K. Inoue, T. Asano, and H. Maeda, *IEEE T. Magn.* **28**, 888 (1992).
16. J. B. Liu, L. Meng, and Y. W. Zeng, *Mat. Sci. Eng. A-Struct.* **435**, 237 (2006).
17. K. Han, A. A. Vasquez, Y. Xin, and P. N. Kalu, *Acta Mater.* **51**, 767 (2003).
18. X. W. Zuo, K. Han, C. C. Zhao, R. M. Niu, and E. G. Wang, *Mat. Sci. Eng. A-Struct.* **619**, 319 (2014).
19. W. A. Spitzig, *Acta Metall. Mater.* **39**, 1085 (1991).
20. G. Bao, Y. Xu, L. Huang, X. Lu, L. Zhang, J. Liu, *et al. Mat. Res. Lett.* **4**, 37 (2016).
21. D. G. Morris, A. Benghalem, and M. A. Morris-Munoz, *Scripta Mater.* **41**, 1123 (1999).
22. Y. Sakai and H. J. SchneiderMuntau, *Acta Mater.* **45**, 1017 (1997).
23. Y. T. Ning, X. H. Zhang, and J. Zhang, *Rare Metal Mat. Eng.* **34**, 1930 (2005).
24. Y. Z. Tian, S. D. Wu, Z. F. Zhang, R. B. Figueiredo, N. Gao, and T. G. Langdon, *Acta Mater.* **59**, 2783 (2011).
25. Y. Sakai, T. Hibaru, K. Miura, A. Matsuo, K. Kawaguchi, and K. Kindo, *MRS Advances* **1**, 1137 (2015).
26. I. Manna, *Interface Sci.* **6**, 113 (1998).
27. W. Grünberger, M. Heilmaier, and L. Schultz, *Int. J. Mater. Res.* **93**, 58 (2002).
28. C. Zhao, X. Zuo, E. Wang, R. Niu, and K. Han, *Mat. Sci. Eng. A-Struct.* **652**, 296 (2016).
29. H. Witte, A. Gaganov, N. Kozova, J. Freudenberger, and H. Jones, *IEEE T. Appl. Supercon.* **16**, 1680 (2006).
30. W. Piyawit, W. Z. Xu, S. N. Mathaudhu, J. Freudenberger, J. M. Rigsbee, and Y. T. Zhu, *Mat. Sci. Eng. A-Struct.* **610**, 85 (2014).
31. L. Zhang, L. Meng, and J. B. Liu, *Scripta Mater.* **52**, 587 (2005).
32. X. W. Zuo, R. Guo, B. L. An, L. Zhang, and E. G. Wang, *Acta Metall. Sin.* **52**, 143 (2016).
33. J. B. Liu, L. Zhang, Y. W. Zeng, and L. Meng, *Scripta Mater.* **64**, 665 (2011).
34. X. Zuo, R. Guo, C. Zhao, L. Zhang, E. Wang, and K. Han, *J. Alloy. Compd.* **676**, 46 (2016).
35. T. Asano, Y. Sakai, S. Matsumoto, T. Kiyoshi, H. Yoshioka, K. Watanabe, *et al. IEEE T. Appl. Supercon.* **18**, 567 (2008).
36. J. C. Malzahn Kampe and T. H. Courtney, *Scripta Metall. Mater.* **20**, 285 (1986).
37. L. Qu, E. Wang, X. Zuo, L. Zhang, and J. He, *Mat. Sci. Eng. A-Struct.* **528**, 2532 (2011).
38. J. D. Verhoeven, S. C. Chueh, and E. D. Gibson, *J. Mater. Sci.* **24**, 1748 (1989).
39. J. P. Ge, H. Zhao, Z. Q. Yao, and S. H. Liu, *T. Nonferr. Metal Soc.* **15**, 971 (2005).
40. J. M. Denney, *Acta Metall. Mater.* **4**, 586 (1956).
41. G. Shi, X. Chen, H. Jiang, Z. Wang, H. Tang, and Y. Fan, *Mat. Sci. Eng. A-Struct.* **636**, 43 (2015).
42. X. Zuo, L. Qu, C. Zhao, B. An, E. Wang, K. Han, *et al. J. Alloy. Compd.* **662**, 355 (2016).
43. G. Mazzone and M. V. Antisari, *Phys. Rev. B* **54**, 441 (1996).
44. R. Monzen and M. Mori, *Phil. Mag. Lett.* **75**, 351 (1997).
45. M. Kato, R. Monzen, and T. Mori, *Acta Metall. Mater.* **26**, 605 (1978).
46. G. Dublon, F. Habbal, and J. Bevk, *Appl. Phys. Lett.* **39**, 659 (1981).
47. E. Wang, L. Qu, X. Zuo, L. Zhang, and J. He, *Metall. Res. Technol.* **110**, 289 (2013).
48. L. Qu, E. Wang, K. Han, X. Zuo, L. Zhang, J. He, *et al. J. Appl. Phys.* **113**, 173708 (2013).
49. N. D. Stepanov, A. V. Kuznetsov, G. A. Salishchev, N. E. Khlebova, and V. I. Pantsyrny, *Mat. Sci. Eng. A-Struct.* **564**, 264 (2013).
50. K. M. Liu, D. P. Lu, H. T. Zhou, Z. B. Chen, A. Atrens, and L. Lu, *Mat. Sci. Eng. A-Struct.* **584**, 114 (2013).
51. G. H. Bao, C. X. Chen, L. Y. Huang, H. Gu, L. Meng, J. B. Liu, *et al. Mat. Sci. Eng. A-Struct.* **655**, 86 (2016).
52. J. S. Huang, D. W. Yao, and L. Meng, *Met. Mater. Int.* **19**, 225 (2013).
53. H. Gao, J. Wang, D. Shu, and B. Sun, *Mat. Sci. Eng. A-Struct.* **452-453**, 367 (2007).
54. Y. F. Wang, H. Y. Gao, Y. F. Han, Y. B. Dai, J. Wang, and B. D. Sun, *J. Alloy. Compd.* **691**, 992 (2017).
55. J. S. Song, S. I. Hong, and H. S. Kim, *J. Mater. Process. Tech.* **113**, 610 (2001).
56. K. Liu, Z. Huang, X. Zhang, D. Lu, A. Atrens, W. Guo, *et al. Mat. Sci. Eng. A-Struct.* **673**, 1 (2016).
57. H. Gao, J. Wang, D. Shu, and B. Sun, *Scripta Mater.* **53**, 1105 (2005).
58. X. Zuo, K. Han, C. Zhao, R. Niu, and E. Wang, *J. Alloy. Compd.* **622**, 69 (2015).
59. D. A. Porter and K. E. Easterling, *Phase Transformations in Metals and Alloys*, pp.196-197, Van Nostrand Reinhold, USA (1981).

60. J. S. Song, S. I. Hong, and Y. G. Park, *J. Alloys Compd.* **388**, 69 (2005).
61. A. Gaganov, J. Freudenberger, E. Botcharova, and L. Schultz, *Mat. Sci. Eng. A-Struct.* **437**, 313 (2006).
62. J. B. Liu, L. Zhang, A. P. Dong, L. T. Wang, Y. W. Zeng, and L. Meng, *Mat. Sci. Eng. A-Struct.* **532**, 331 (2012).
63. J. B. Liu, L. Zhang, and L. Meng, *Mat. Sci. Eng. A-Struct.* **498**, 392 (2008).
64. Y. T. Ning, X. H. Zhang, and Y. J. Wu, *Rare Metal Mat. Eng.* **36**, 1425 (2007).
65. H. L. Zhao, J. S. Yue, Y. Gao, and K. R. Weng, *Rare Metals* **32**, 12 (2013).
66. C. Zhao, X. Zuo, E. Wang, and K. Han, *Met. Mater. Int.* **23**, in press (2017).
67. N. J. Petch, *J. Iron Steel Res. Int.* **174**, 25 (1953).
68. E. O. Hall, *P. Phys. Soc. Lond. B* **64**, 747 (1951).
69. S. I. Hong, *Adv. Eng. Mater.* **3**, 475 (2001).
70. D. Raabe, S. Ohsaki, and K. Hono, *Acta Mater.* **57**, 5254 (2009).
71. M. Murayama, A. Belyakov, T. Hara, Y. Sakai, K. Tsuzaki, T. Kimura, *et al. J. Electron. Mater.* **35**, 1787 (2006).
72. J. Freudenberger, J. Lyubimova, A. Gaganov, H. Witte, A. L. Hickman, M. Nganbe, *et al. Mat. Sci. Eng. A-Struct.* **527**, 2004 (2010).
73. Z. X. Xie, H. Y. Gao, Q. Lu, J. Wang, and B. D. Sun, *J. Alloy. Compd.* **508**, 320 (2010).
74. J. Bevk, *Annu. Rev. Mater. Sci.* **13**, 319 (1983).
75. F. Bittner, S. Yin, A. Kauffmann, J. Freudenberger, H. Klauss, L. Schultz, *et al. Mat. Sci. Eng. A-Struct.* **597**, 139 (2014).
76. V. M. H. Lopez and K. Hirano, *J. Mater. Sci.* **29**, 4802 (1994).
77. A. M. Wusatowska-Sarnek, H. Miura, and T. Sakai, *J. Mater. Sci.* **34**, 5477 (1999).